Supplemental Information

Biomechanics of *Borrelia burgdorferi*

Vascular Interactions

Rhodaba Ebady, Alexandra F. Niddam, Anna E. Boczula, Yae Ram Kim, Nupur Gupta, Tian Tian Tang, Tanya Odisho, Hui Zhi, Craig A. Simmons, Jon T. Skare, and Tara J. Moriarty

SUPPLEMENTAL INFORMATION

SUPPLEMENTAL DATA ITEMS

SUPPLEMENTAL MOVIES, FIGURES AND LEGENDS

Movies S1-S4: *Related to Figure 1.*

B. burgdorferi interactions with human endothelia in flow chambers and postcapillary venules of live mice.

GFP-expressing infectious GCB966 **(Movies S1, S3)** and non-infectious GCB706 **(Movies S2, S4)** interacting with post-confluent HUVEC counterstained with plasma membrane dye (red) at 1 dyn/cm^2 in flow chambers (Movies S1, S2: scale bar: 21 µm), and with dermal postcapillary venules (PCVs) counterstained with AlexaFluor555-PECAM-1 antibody (Movies S3, S4: scale bar: 32 µm). All movies were acquired and exported at 15 frames per second.

Movie S1: GCB966 flow chamber
Movie S2: GCB706 flow chamber
Movie S3: GCB966 PCV
Movie S4: GCB706 PCV

Figure S1: *Related to Figure 1.*

Optimization of infectious B. burgdorferi dragging interactions with human endothelia in flow chambers at 1 dyn/cm^2.
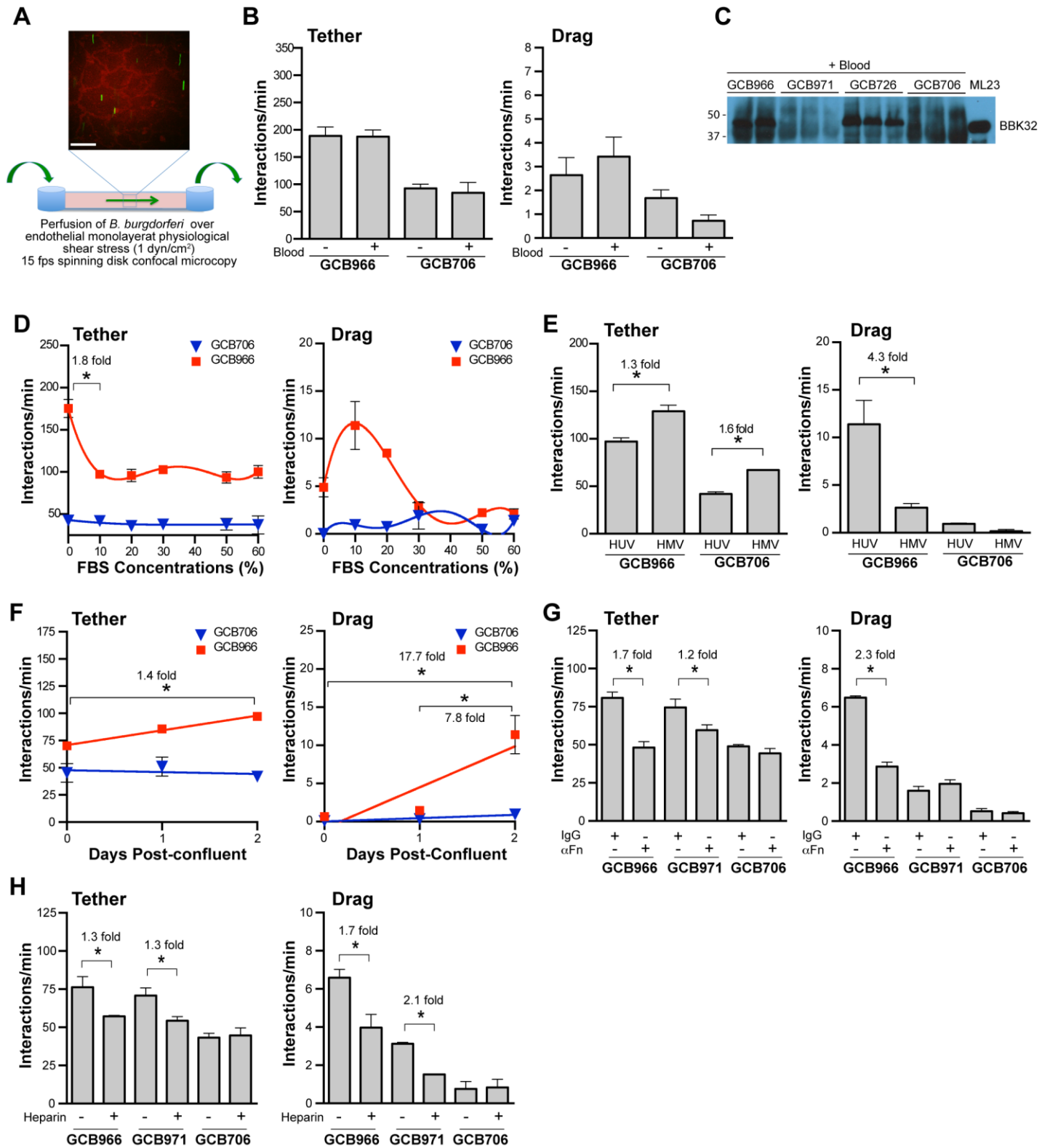
(A) Flow chamber model system. GFP-expressing *B. burgdorferi* (GCB966) interacting with HUVEC (red, labelled with plasma membrane dye) in flow chamber. Frame from green channel time lapse recording is overlaid on micrograph in which junctions are most sharply focused. Scale bar: 42 μm.

(B, D-F) The final optimized conditions used in all experiments reported in Figures 1-6 and S2-S5 were: 48 h cultivation of bacteria in 1% mouse blood (B), perfusion of bacteria in saline containing 10% fetal bovine serum (FBS: D) over HUVEC (HUV: E) cultivated to

2 days post-confluence (F). In E, HUV were compared to primary human dermal microvascular endothelial cells (HMV). Unless otherwise noted, experiments were performed with bacteria cultivated in mouse blood, 10% FBS in perfusion medium, and 2d post-confluent HUVEC.

(C) BBK32 expression in independent *B. burgdorferi* inocula cultivated in 1% mouse blood. <u>Bacterial strains</u>: *bbk32*-null GCB706 and GCB966-derived GCB971, BBK32-expressing GCB726 and GCB966, and ML23 positive control strain grown in the absence of blood. Background reactivity to blood in culture medium is visible for all samples except ML23. At left: positions of molecular mass markers (kDa).

(G-H) *B. burgdorferi*-endothelial interactions in the presence of polyclonal anti-fibronectin IgGs and pre-immune control IgGs (G), and in the presence of competitive inhibitor heparin (H)

<u>Summary values (all panels)</u>: mean ± SEM.

<u>Replicates</u>: N≥3 replicates/strain and experimental condition.

<u>Statistics</u>: two-way ANOVA, Holm-Sidak post-test. *p<0.05.

Figure S2: *Related to Figure 2.*

Frequencies and dissociation rates of B. burgdorferi-endothelial interactions.
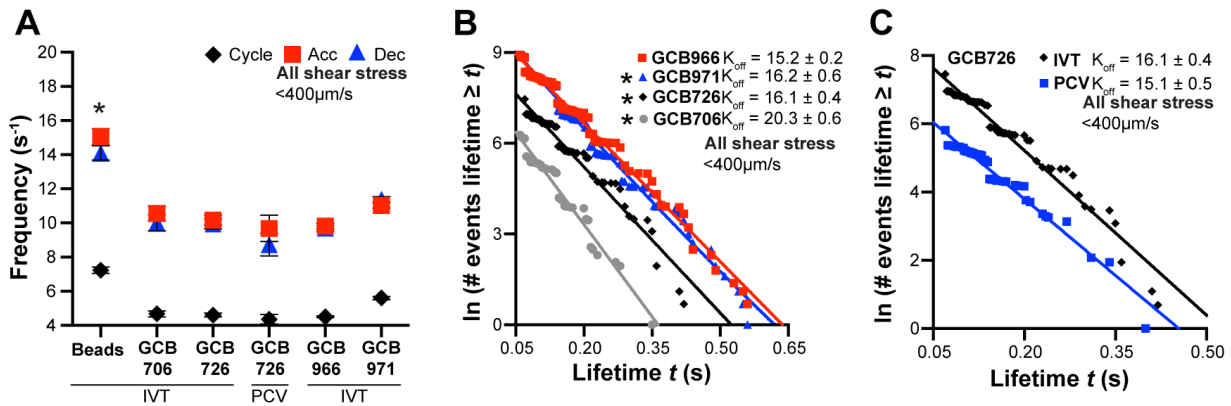
(A) Global mean ±95% CI frequency of whole cycles and acceleration and deceleration phases. For all interaction categories (acc, dec, cycle), *p<0.05 vs all groups for beads.

(B-C) Frequency distribution of log-transformed deceleration phase bond lifetimes (*t*) in flow chambers (B, and C: IVT) and in PCVs (C). $R^2>0.9$ for all curves. Dissociation rates (K_{off}) estimated from negative slopes of linear frequency distributions are provided for each strain and condition. *p<0.05 vs GCB966.

<u>Replicates</u>: IVT: N≥27 replicates/strain (≥3 independent replicates/shear stress); PCVs: ≥16 mice/strain. **Table S2**: numbers of tracks and interactions analyzed in each experiment.

<u>Statistics</u>: two-way ANOVA, Holm-Sidak post-test.

Figure S3: *Related to Figure 3.*

Bacterial conformation under no-flow and low-flow conditions.
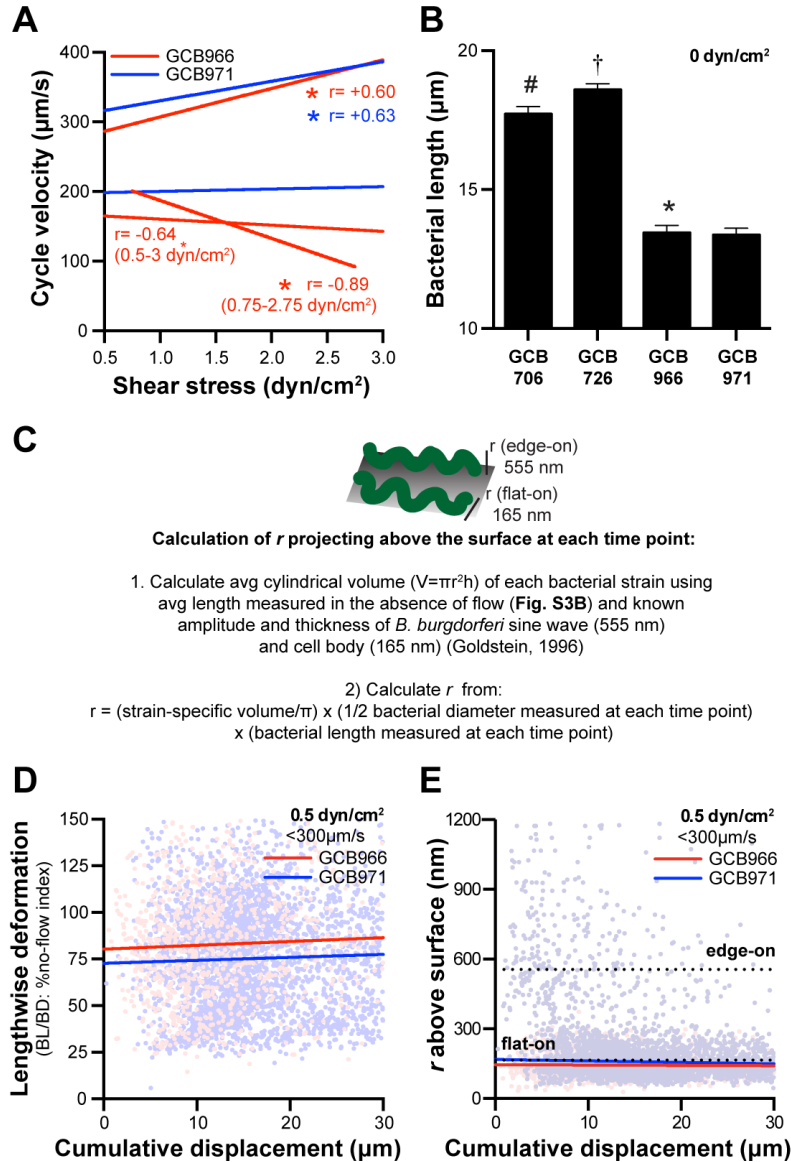
(**A**) Linear regression and correlation analysis of effect of increasing shear stress on interaction cycle velocity. Top: interactions with velocities 300-400 µm/s (0.5-3 dyn/cm^2). Bottom: velocities <300 µm/s (0.5-3 dyn/cm^2, and 0.75-2.75 dyn/cm^2). *p<0.05 velocity vs. shear stress, r=Spearman correlation coefficient. All experiments reported from Figure 3 and S3D onward were conducted with interactions with cycle velocities <300 µm/s.

(**B**) Mean ± 95% CI bacterial length for all strains under no flow, static conditions (3 independent cultures). *p<0.05 GCB966 vs. GCB706 and GCB726, #p<0.05 GCB706 vs. all groups, †p<0.05 GCB726 vs. all groups. N = 107, 137, 55 and 72 measured bacteria for GCB706, GCB726, GCB966 and GCB971, respectively (two-way ANOVA with Holm-Sidak post-test).

(**C**) Method used to calculate instantaneous bacterial radius (*r*) projecting above endothelial surface during interactions.

(**D-E**) Non-linear regression analyses of changes in bacterial lengthwise deformation (D) and projection above endothelial surfaces (E) with increasing displacement during interactions.

<u>Replicates:</u>**Table S2**: numbers of tracks and interactions analyzed in each experiment.

A

Shear rate (γ)

r = cell radius projecting above surface
T_s = 11.87 $\tau_w r^3$ (torque due to flow)
F_N = normal force
F_s = 31.97 $\tau_w r^2$ (force due to flow)
F_b = $F_s/\cos\theta$ (force on load-bearing bond)

ℓ = lever arm length
R = $\sqrt{r^2 + \ell^2}$
τ_w = wall shear stress
θ = bond angle

T_s

F_s

F_b

θ

tether + adhesion complex

F_N

r

ℓ (deceleration displacement)

B
T_s (pN nm)
All shear stress
<300μm/s
GCB966
GCB971
Bacterial length (μm)

C
F_s (pN)
All shear stress
<300μm/s
GCB966
GCB971
F_m
Bacterial length (μm)

D
T_s (pN nm)
All shear stress
<300μm/s
GCB966
GCB971
*

E
F_s (pN)
All shear stress
<300μm/s
GCB966
GCB971
F_m
*

F
Bond angle (°)
0.75-3 dyn/cm²
<300μm/s
GCB966
GCB971
Cumulative displacement (μm)

G
Bond angle (°)
All shear stress
<300μm/s
GCB966
GCB971
Bacterial length (μm)

H
Bond angle (°)
All shear stress
<300μm/s
GCB966
GCB971
*

I
Relative frequency (%)
All shear stress
<300μm/s
GCB966
GCB971
Bond angle (°)

Figure S4: *Related to Figure 4.*

Bond angles, and torque (T_s) and force due to flow (F_s) for bacteria interacting with endothelia under shear stress

(A) Formulas used to estimate torque (T_s) and force due to flow (F_s) imposed on bacteria (treated as cylinders), bond angle (θ) and force on individual load-bearing bonds (F_b).

(B-E) Torque (B: T_s) and force due to flow (C: F_s) for interactions binned by bacterial length, and global mean values (D-E). F_m: estimated *B. burgdorferi* propulsive force generated by bacterial motility. For GCB966 and GCB971, which are ~13.4 µm long, $F_m \approx 4\pi$(bacterial length: 13.4 µm)(bacterial swim speed in liquid media with the viscosity of saline: 4.25 µm/s), or ≈ 0.72 pN (Goldstein et al., 1994; Wolgemuth, 2008).

(F-I) Bond angles. Non-linear regression analyses of changes in bond angle with increasing displacement during interaction (F). Average bond angle for interactions binned by bacterial length (G). Global mean bond angle (H). Frequency distribution of different bond angles.
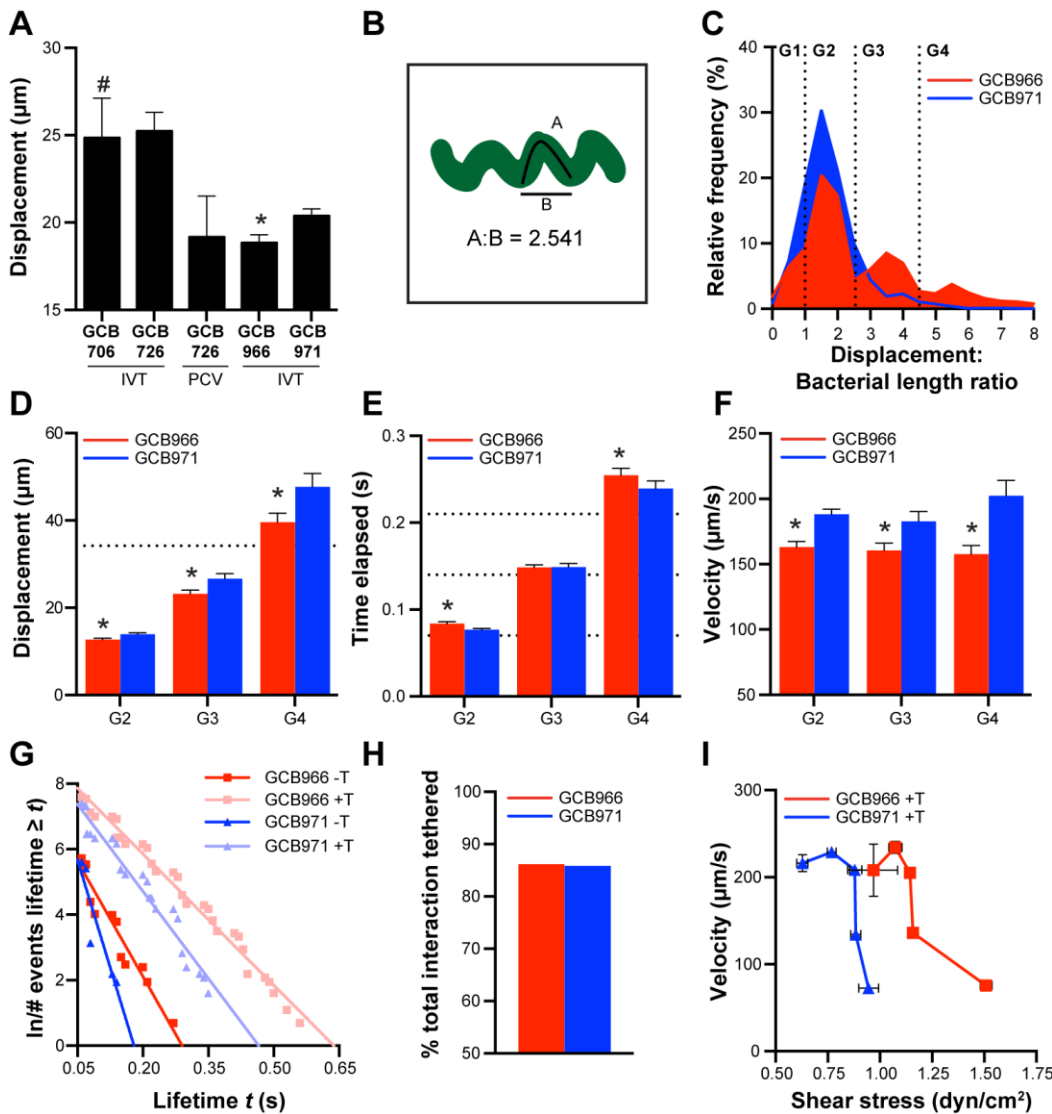
Summary values: mean±95% CI.

Replicates: **Table S2**: numbers of tracks and interactions analyzed in each experiment.

Statistics: two-way ANOVA, Holm-Sidak post-test. *$p<0.05$ GCB966 vs GCB971.

6

Figure S5: *Related to Figure 5.*

Displacement, duration, dissociation rates and velocities for tethered (+T) and untethered (-T) interactions: all shear stress conditions

(A) Average displacement during interactions under flow, which was greater than the average bacterial length for each strain under no-flow conditions (**Figure S3B**). *p<0.05 GCB966 vs. GCB706, GCB726, GCB971; #p<0.05 GCB706 vs. GCB966, GCB971, GCB726 PCV.

(B) Approach used to distinguish tethered from untethered interactions. The *Borrelia* outer membrane is fluid and most adhesins are lipoproteins (Bergström and Zückert, 2010). Thus, displacement beyond the end-to-end length of bacteria (~13.4 µm for GCB966 and GCB971) could possibly be due to dragging of adhesins along the surface contours of the bacterial sine wave, causing bacteria to appear to displace further than their end-to-end length. As illustrated in (B), the ratio of the contour length of bacteria is 2.541 times the distance between successive peaks of the bacterial sine wave (2.83 µm) (Goldstein et al., 1996). Interactions in which bacteria displace more than 2.541 times their end-to-end length (34 µm for GCB966 and GCB971) displace further than is consistent with adhesion complex dragging along bacterial contours, and are likely anchored by tethers.

(**C-F**) Properties of interactions with distinct ratios of displacement to bacterial length under flow. (C) Frequency distribution of interactions with different ratios. Identified groups: G1 (≤1), G2 (>1<2.541), G3 and G4 (>2.541). (D) G4 interactions travelled further than 34 µm, and were thus tethered. G2-G4 interactions displaced successively further, but were also progressively longer-lived (E), with average lifetimes clustering near the most common image acquisition time increments (0.07, 0.14 and 0.21s). (F) G2-G4 velocities were indistinguishable within each strain (p>0.05), indicating that progressively greater displacements in G2-G4 (D) were a function of increasing time elapsed in each of these groups (E), and that G2-G4 groups corresponded to the same type of interaction. We concluded that interactions in which bacteria travelled less than their length under flow were untethered (-T: G1), whereas those which travelled further than their length were tethered (+T: G2-G4). *p<0.05 GCB966 vs GCB971

(G) Frequency distribution of log-transformed deceleration phase bond lifetimes (*t*) for tether-independent (-T) and tether-dependent (+T) interactions.

(H) % of all interactions which are +T.

(I) Velocity of +T interactions at indicated shear stresses.

Summary values: mean ±95% CI.

Replicates: **Table S2**: numbers of tracks and interactions analyzed in each experiment.

Statistics: two-way ANOVA, Holm-Sidak post-test.

SUPPLEMENTAL TABLES

Table S1: *B. burgdorferi strains used in this study*

Strain number	Background	Description	Reference
GCB706	B31-A	B31-A/pTM61 (same as GCB705 but clone 2); non-infectious high passage B31-A derivative containing P_{flaB}-driven GFP expression plasmid pTM61; missing plasmids lp21, lp25, lp28-1, lp28-4, lp36, cp9 and cp32-6	(Moriarty et al., 2012, 2008)
GCB726	B31 5A4 NP1	5A4NP1/pTM61 (clone 2); infectious **BBK32-expressing** B31 derivative containing P_{flaB}-driven GFP expression plasmid pTM61. Contains all endogenous plasmids except cp9 which was replaced by cp9-based pTM61	(Moriarty et al., 2008)
GCB966	B31 derivative ML23 (ML23/pJW201)	ML23/pJW201; infectious **BBK32-expressing** ML23-derived strain expressing P_{flaB}-driven GFP, missing lp25 and reconstituted with *bbe22* locus encoding nicotinamidase carried on plasmid pJW201(P_{flaB}-GFP/bbe22)	(Moriarty et al., 2012; Seshu et al., 2006; Wu et al., 2011)
GCB971	ML23 derivative $bbk32::str^R$ (JS315/pJW201)	ML23-derived $bbk32::str^R$ *bbk32* strain expressing P_{flaB}-driven GFP on plasmid pJW201(PflaB- GFP/bbe22); isogenic parent: GCB966(Moriarty et al., 2012; Wu et al., 2011)(Moriarty et al., 2012; Wu et al., 2011). **Does not express BBK32**.	(Moriarty et al., 2012; Seshu et al., 2006; Wu et al., 2011)

Table S2: *Numbers of trajectories and interactions analyzed in reported experiments*

	Number of trajectories analyzed						Number of interactions analyzed					
	Flow chambers					PCVs	Flow chambers					PCVs
Experiment	Beads	GCB 706	GCB 726	GCB 966	GCB 971	GCB 726	Beads	GCB 706	GCB 726	GCB 966	GCB 971	GCB 726
Fig. 1C-D	121	210	679	2,721	--	96	--	--	--	--	--	--
Fig. 2C-D, S2A	121	210	679	2,721	2,493	96	--	--	--	--	--	--
Fig. 2E-F, S2B-C, S3A	--	210	679	2,721	2,493	96	--	510	1,246	4,337	3,251	458
Fig. 3B, F, 5A, S5A	--	--	--	--	--	--	--	164	899	2,542	2,812	323
Fig. S3D-E	--	--	--	--	--	--	--	--	--	184	1,881	--
Fig. 3C, G, S4F	--	--	--	--	--	--	--	--	--	2,358	931	--
Fig. 3D-E, H, 4B-E, 5C-D, S4B-E, G-I, S5C, H	--	--	--	--	--	--	--	--	--	2,303	1,930	--
Fig. 3I-J	--	--	--	--	--	--	--	--	--	305	273	--
Fig. S5D-E	--	--	--	--	--	--	--	--	--	1,998	1,657	--

-- not applicable

EXTENDED EXPERIMENTAL PROCEDURES

EXTENDED EXPERIMENTAL PROCEDURES

ENDOTHELIAL CELL CULTIVATION AND LABELLING FOR FLOW CHAMBER LIVE CELL IMAGING EXPERIMENTS

Early passage primary human umbilical vein endothelial cells (HUVEC, Clonetics) and human neonatal foreskin dermal microvascular endothelial cells from small blood vessels and lymphatics in healthy skin (HMVEC-d, Clonetics) pooled from multiple donors were purchased from Lonza (Allendale, NJ ; cat # CC-2519A and CC-2516 respectively). Cells were cultured in tissue culture-treated T75 flasks without gelatin or fibronectin coating according to manufacturer's instructions, in EGM-2 medium (cat# CC-3156) supplemented with bullet kits recommended for each cell line (cat # CC-4176 and CC- 4147, respectively). Composition of HUVEC and HMVEC-d bullet kits was similar (FBS, hydrocortisone, hFGF-B, VEGF, R3-IGF-1, ascorbic acid, hEGF, GA-1000) except that the HUVEC bullet kit also contained heparin, and heat-inactivated fetal bovine serum (FBS) was added to a final concentration of 2% for HUVEC and 5% for HMVEC-d (concentrations of other components is proprietary). Cells were passaged at ~80% confluence after rinsing with 37°C phosphate buffered saline (Multicell Wisent, St-Bruno, QC), trypsinized with pre-warmed trypsin (0.05% trypsin/0.53 mM EDTA; Life Technologies, Burlington, ON) for 5 min at 37°C, and neutralized with complete medium, followed by centrifugation at 220 xg for 5 min and resuspension in fresh complete medium. Cultures were maintained in a humidified atmosphere containing 5% CO_2 at 37°C. All experiments were conducted with early passage cells (up to a maximum of 5 passages). Cells were frozen after trypsinization and neutralization by resuspension in whole medium containing 1% dimethyl sulfoxide (DMSO; Bioshop Canada, Burlington, ON) and 20% FBS (Sigma-Aldrich Canada, Oakville, ON).

For cultivation in flow chambers, cells were re-suspended in appropriate medium to a density of ~5.3 x 10^6cells/ml and 30 µL of this suspension was plated into each channel of an ibiTreat hydrophilic tissue-culture treated Ibidi µ-Slide VI$^{0.4}$ (6 channels/slide, height x length x width of each channel: 0.4 x 17 x 3.8 mm; thickness and refractive index of imaging surface: 180 µm and 1.52, respectively) (Ibidi GmbH, Planegg, Martinsried, Germany), followed by addition of 60µL of appropriate cultivation medium. Chambers were not coated with gelatin or fibronectin before cell plating. At this plating density, cells reached confluence (as determined by phase contrast microscopy) within 16 hours. For experiments conducted with endothelia at 0 days post-confluence, cells were cultivated in the Ibidi slide overnight before imaging the following morning. Experiments conducted with cells at 1 and 2 days post-confluence were cultivated for an additional 1 and 2 days, respectively, before imaging. Once cells were plated in Ibidi slides, culture medium was changed daily.

Immediately before addition of bacteria and imaging of endothelial-bacterial interactions in flow chambers, endothelial cells were labelled for 5 min at 37°C with 100 µl of a 1 in 2000 dilution of CellMask Deep Red plasma membrane live cell imaging amphipathic dye prepared in endothelial growth medium according to manufacturer instructions (Life Technologies), followed by rinsing with HBSS perfusion medium to remove unincorporated dye.

B. BURGDORFERI STRAINS, CULTIVATION, HOST ADAPTATION AND PREPARATION FOR IMAGING

GCB726 is a previously reported B31 5A4 NP1-derived infectious strain transformed with GFP-expressing plasmid pTM61 (Moriarty et al., 2008). GCB706 is a previously reported B31-A-derived non-infectious high passage strain transformed with GFP-expressing plasmid pTM61 (Moriarty et al., 2012). GCB966 is a previously reported B31-derived ML23 infectious strain (Seshu et al., 2006) transformed with GFP-expressing pJW201 (P_{flaB}-GFP/*bbe22*) (Wu et al., 2011). GCB971 is a previously reported ML23-derived *bbk32::str^R bbk32* knockout strain (Seshu et al., 2006) transformed with the GFP-expressing plasmid pJW201 (P_{flaB}-GFP/*bbe22*) (Wu et al., 2011).

All strains were grown in BSK-II medium prepared in house (Barbour, 1984) containing 6% rabbit serum (Cedarlane Laboratories, Burlington, ON) and 100 µg/ml gentamycin (Bioshop) at 36°C and 1.5% CO_2. Cultivation, host adaptation and preparation of *B. burgdorferi* for imaging were performed as described previously (Moriarty et al., 2008). Freshly inoculated cultures grown for 4-5 days were diluted to 2×10^6/ml 48 h before experiments, in complete growth medium containing 100 µg/ml gentamycin, 20 µg/ml phosphomycin (Sigma-Aldrich), 50 µg/ml rifampicin and 2.5 µg/ml amphotericin (Bioshop), and cultivated to $0.5-1 \times 10^8$/ml before imaging. Blood for host adaptation was obtained by cardiac puncture from C57BL/6 mice (Charles River Laboratories, Montréal, QC) anesthetized with 10 mg/kg xylazine (MTC Pharmaceuticals, Cambridge, ON) and 200 mg/kg ketamine hydrochloride (Rogar/STB, Montréal, QC), using needles and syringes coated with 20 µl 100 U/ml heparin (Sigma) and added to cultures 48h before imaging at 1% final concentration. In experiments performed without host adaptation, cultivation medium and antibiotics added were identical for cultures with and without blood.

On the day of flow chamber imaging, bacteria were centrifuged at 5000 xg 4°C for 15 min, washed twice with 20 ml ice-cold PBS and resuspended to 4×10^8/ml in PBS. Bacteria were stored on ice until imaging, when they were diluted to 1×10^8/ml in room temperature Hank's Balanced Salt Solution (HBSS: Life Technologies) containing 10% heat-inactivated FBS. Bacterial suspensions were warmed to room temperature before perfusion over endothelial monolayers in flow chambers. For intravital microscopy, washed bacteria were suspended to 2×10^9 *B. burgdorferi*/ml in PBS, and stored on ice until injection (after warming to room temperature). For both flow chamber and intravital imaging, bacterial suspensions were passed through an 18G needle before perfusion or intravenous injection, to ensure dissociation and removal of any bacterial clumps and/or blood clots remaining after washing.

IMMUNOBLOTTING DETECTION OF BBK32 EXPRESSION

Expression levels of BBK32 were measured in independent GCB706, GCB726, GCB966 and GCB971 *B. burgdorferi* cultures cultivated and processed under the same conditions as those used for imaging (i.e. in presence of 1% mouse blood for 48h, followed by PBS washing). Samples corresponding to 10^8 whole cell equivalents were separated by SDS-PAGE and immunoblotted using polyclonal antiserum to BBK32 (courtesy Seppo Meri, University of Finland). Strain ML23 grown at 37°C, pH 6.8 was used as a positive control for RpoS-dependent induction of *bbk32* (Zhi et al., 2015).

PREPARATION OF CONTROL BEADS FOR FLOW CHAMBER IMAGING

A 0.083% w/v suspension of orange fluorescent 1.0 µm carboxylate-modified microspheres (Ex/Em 540/560 nm) (FluoSpheres, Molecular Probes, Life Technologies Inc., Burlington, ON) was perfused over endothelial monolayers in triplicate experiments at each of 0.5, 0.75, 1, 1.25, 1.75, 2, 2.25, 2.75 and 3 dyn/cm^2 after the following preparations. The bead stock (2% w/v) was vortexed at maximum speed for one min, followed by centrifugation of 500 µl of beads at 17,900 xg for 15 min, resuspension and vortexing in 500 µl of PBS, addition of BSA to a final concentration of 1 mg/ml, and incubation at RT°C for 60 min with gentle shaking. The resulting solution was passed through an 18G needle, diluted to a final volume of 60 ml with HBSS and sonicated for 2-5 sec before perfusion through flow chambers.

FLOW CHAMBER PERFUSION CONDITIONS

Sterile 10 or 60 ml syringes containing suspensions of *B. burgdorferi* in warmed perfusion medium were connected to flow chamber inlets via silicon tubing (1.6 and 3.2 mm inner and outer diameter, respectively) and 1.6/3.2 mm elbow adaptors (Ibidi GmbH, Planegg, Martinsried, Germany), then placed in a syringe pump apparatus (Model: NE1000, New Era Pump Systems Inc., Farmingdale, NY). Chambers connected to the syringe pump were mounted in a stage-top live cell imaging incubator with cover, main body, humidifier and lens warmer temperatures set to 37.5, 37.5, 45 and 39°C, respectively (CU109 Chamlide TC, LCI Live Cell Instruments, Nowon-gu, Seoul, Korea). Perfusion was begun as soon as flow chambers were placed in the incubator. Syringe pump flow rates used to achieve wall shear stresses of 0.5, 0.75, 1.0, 1.25, 1.75, 2.0, 2.25, 2.75 and 3 dyn/cm^2 were calculated using the formula provided by the flow chamber manufacturer (τ[dyn/cm^2] = 1.761φ[ml/min], where τ is shear stress in dyn/cm^2 and φ is flow rate in ml/min), and were 0.284, 0.426, 0.568, 0.710, 0.994, 1.136, 1.28, 1.56 and 1.704 ml/min, respectively. For flow rate calculations, we assumed the same dynamic viscosity for all experimental conditions, independent of FBS concentration or presence of blood in perfusion medium (dynamic viscosity of water at 22°C: 1 cP). Syringe diameter parameters were 14.5 and 26.7 mm for 10 and 60 ml syringes, respectively.

POLYCLONAL αFN ANTIBODY BLOCKING AND HEPARIN COMPETITION

Bacteria were cultivated in 1% mouse blood for 48 h, prepared for imaging as described above, resuspended to 2.5 x 10^9/ml in PBS, and 0.4 ml of this suspension was incubated for 60 min at RT°C with non-specific goat IgGs or polyclonal goat anti-rabbit pFn IgGs added to a final concentration of 1 mg/ml. (Cappel/MP Biomedicals Canada; cat #55632, 64143 respectively). After incubation, bacteria and antibodies were diluted into HBSS perfusion medium containing 10% FBS to 1 x 10^8 *B. burgdorferi/*ml without removal of antibody. Bacteria were perfused over HUVEC at 1 dyn/cm^2. For heparin competition, 0.4 ml of bacterial suspension was incubated with either 50 µg/ml of heparin sodium from porcine mucosa (Sigma; cat # SRE0027) or the same volume of PBS control for 30 minutes at 4°C with agitation. After incubation, bacteria and heparin were diluted into HBSS perfusion medium containing 10% FBS to 1 x 10^8 *B. burgdorferi/*ml. Bacteria were perfused over HUVEC at 1 dyn/cm^2.

INTRAVITAL MICROSCOPY SURGICAL PREPARATIONS, INTRAVENOUS INJECTIONS AND VASCULAR LABELLING

The intravital microscopy experiments described in this manuscript were conducted during previous studies (Moriarty et al., 2012, 2008). Interaction rate data reported in Fig. 1F and 2B are compilations of interaction rates calculated in previously published studies and are provided for reference. All tracking analysis of intravital microscopy data reported in the current manuscript is novel. As previously described in detail (Moriarty et al., 2012, 2008), intravital microscopy was performed in surgically prepared flank skin following intravenous inoculation via tail or jugular vein of 5 x 10^8 host-adapted washed *B. burgdorferi* resuspended to 2 x 10^9 bacterial/ml in PBS, and vessel counterstain (50 µl of 0.02% 70 kDa Texas Red dextran or 50 µg of AlexaFluor 555-conjugated CD31/PECAM-1 antibody) (Life Technologies; BD Biosciences, Mississauga, ON). For surgical preparations, 5- to 6-week old male C57BL/6 mice (Charles River Laboratories) were anesthetized with 10 mg/kg xylazine and 200 mg/kg ketamine hydrochloride. Following midline dorsal or ventral incisions from the base of the skull to the base of the tail (dorsal) or from the pelvis to the clavicle (ventral), the flank skin was gently separated from underlying connective tissues, reflected and extended over a viewing pedestal using 4.0 sutures to expose the dermal vasculature. Loose connective tissue covering the exposed vasculature was carefully removed by dissection of saline moistened tissues under a stereoscopic microscope, and cleaned tissue was immersed in isotonic saline and covered with a microscope coverslip affixed with vacuum grease. Bacterial-vascular interactions were recorded in straight, unbranched postcapillary venules (diameter 20-50 µm), from 5-25 minutes following intravenous injection of bacteria.

MICROSCOPY CONDITIONS

Flow chambers

Spinning disk confocal microscopy was performed using a custom-built Quorum Spinning Disk Confocal microscope (Quorum Technologies Inc., Guelph, ON) installed at the Hospital for Sick Children Imaging Facility (Toronto, ON), which was equipped with a Zeiss Axiovert 200M inverted fluorescence microscope (Carl Zeiss Canada, Toronto, ON), Hamamatsu C9100-13 512 x 512 pixel back-thinned C9100-13 EM-CCD Camera (Hamamatsu, Bridgewater, NY), Yokogawa CSU-10 spinning disk confocal scan head (Yokogawa Electric Corporation, Tokyo, Japan), LMM5 laser merge module and 50 mW 491 and 561 nm pumped diode lasers (Spectral Applied Research, Richmond Hill, Ontario). Images were acquired at 16 bits/channel without binning using a Zeiss 25x/0.8 NA LCI Plan-Apochromat water immersion lens (Carl Zeiss) at an xy resolution of 0.375 µm/pixel, using a 40 nm bandwidth GFP emission filter centered at 515 nm and 40 nm bandwidth Texas Red emission filter centered at 624 nm (Semrock Inc., Rochester NY). Microscope control and image acquisition were performed using Volocity software v.6.3.0 (Improvision/Perkin-Elmer, Waltham, MA) at 100% laser power and transmission and maximum sensitivity range (0-255) in both red and green channels (except for bead experiments, where laser power was reduced to the lowest settings possible to reduce image saturation). Exposure times in the red channel (beads and endothelia stained with plasma membrane dye) were determined by the auto exposure function (typical exposure times for visualization of endothelia and beads, respectively: 217 and 31 ms), and exposure times in the green channel were optimized for fastest possible acquisition (~70 ms/frame, 14-15 frames/second).

For each flow chamber experiment, one micrograph was first captured of the endothelial monolayer alone to verify monolayer integrity, at the z-position where plasma membrane dye staining of intercellular junctions was sharpest. The z-position was then reset to the position where bacterial interactions with the endothelial monolayer were clearest (usually performed by focusing on a stationary bacterial adhesion in the green channel, typically <10 µm above the position where junctions were most sharply focused). Two minute time lapse series were acquired at 14-15 fps in the green channel. Time courses were captured at the midpoint between chamber inlets and outlets, and left and right chamber walls, to ensure that interactions were measured at the position in chambers where flow is uniform. If focal drifting occurred, manual refocusing was performed to ensure spirochetes interacting with the endothelial cell surface remained in the focal plane. Acquired images and time courses were exported in acff format for offline analysis in Volocity.

Intravital microscopy

Intravital microscopy was performed using a previously described custom-built spinning disk microscope system (Quorum Technologies) (Moriarty et al., 2008) equipped with a 20X 0.95 NA water immersion objective (Olympus, Center Valley, PA), 512x512 back-thinned C9100-13 EMCCD camera (Hamamatsu) and Yokogawa CSU-10 head. Image acquisition at 14-15 fps was achieved by 2X binning, at maximum sensitivity range and laser power, under auto-contrast conditions. Green channel exposure times were 50 ms; red channel exposure times were 30 ms.

POST-ACQUISITION IMAGE PROCESSING

No post-acquisition image processing was performed before tracking analysis. For intravital microscopy videos prepared for presentation, contrast was adjusted and noise was removed with a fine noise filter in Volocity to maximize signal to noise ratios.

All image analysis was performed only for time lapse videos where monolayers were intact and confluent (determined by capturing snapshots of counterstained monolayer in each channel before each experiment), and where bacteria were in the focal plane of the surface of endothelial cells for at least 75% of time lapse duration. Data quality for each time lapse was independently verified by at least two individuals before tracking analysis was performed. Standard deviation in average track velocities within each replicate for any given experimental condition were >38% of the mean, due to the presence of multiple populations of interaction types, whereas standard deviation in average mean velocities of each replicate experiment (comparing average track velocity in each replicate to other replicates) was <14% of the mean. This indicated that imaging and tracking conditions and results were highly reproducible among experimental replicates. Since the major source of variation resulted from variation between individual trajectories within each experimental replicate, all statistical comparisons for tracking data was performed treating individual trajectories (or interactions within each trajectory) as independent replicates, as is standard for analysis of particle-tracking data. The numbers and types of replicates analyzed for each experiment is summarized in **Table S2**.

Manual counting of bacterial-endothelial interaction numbers (Fig. 1A, D, S1B, D-H)

As previously described, *B. burgdorferi* interaction rates were measured in intravital microscopy time courses by counting the number of bacteria/minute that visibly paused but took less than 1 sec to travel 100 µm along the length of a postcapillary venule in the direction of flow (tethering), and those which took more than 1 sec to travel 100 µm (dragging) (Moriarty et al., 2008; Norman et al., 2008). For flow chamber time courses, numbers of interactions which slowed compared to free-flowing bacteria but took less than 1 s to travel 100 µm in the direction of flow through a 30x100 µm region of interest positioned at the centre of the field of view (tethering), or took >1 s to travel 100 µm in the same region of interest (dragging) were counted manually. Since manual counting did not yield information about individual bacteria within each replicate, statistical analysis was performed by treating the counts obtained for each time lapse (i.e. independent biological replicate) as an independent replicate.

Semi-automated tracking of bacteria and bead trajectories

Semi-automated centroid-based tracking was performed using Volocity v.6.3.1. These protocols identified GFP-expressing bacteria based on a combination of object area thresholds and intensity, which were determined empirically during protocol development, followed by automated assembly of objects with similar area and intensity profiles from successive time frames into tracks. Each trajectory identified by automated tracking protocols was visually inspected to ensure that it corresponded to the movement of a single bacterium, and did not result from inappropriate joining of tracks from adjacent but distinct bacteria (a problem most commonly encountered when the trajectory of one bacterium passed immediately adjacent to or over a stationary adhesion). Automatically generated trajectories in which one track was joined to another were manually separated by removal of inappropriately joined objects.

Data output consisted of time lapse projections of all objects tracked over 2 min time courses, and individual measurements for each object at each time point of area (μm^2), skeletal length (µm), skeletal diameter (µm), signal intensity in green channel (arbitrary units, AU: min, max, mean, standard deviation), time/time point (s), displacement (µm) and instantaneous velocity (µm/s). The properties of whole trajectories, including length (µm), time span (s), track velocity (µm/s) and meandering index (sinuosity index, SI) were also automatically calculated by our tracking protocols, but were revised and recalculated in Excel following separation of inappropriately joined tracks (see **Trajectory Analysis Methods** described below). Output data were exported to Excel for further analysis. For each tracking experiment, all trajectories acquired in a time course were visualized in a single time lapse projection image (e.g. **Fig. 1B**).

Tracking protocol for beads

The brightest ~10% of objects corresponding to those closest to the focal plane within a defined region of interest (whole field of view) which were not touching the edge of the field of view and had an area between 5-200 μm^2 were identified and tracked over 2 min time courses. Although the diameter of beads was 1 μm^2, their extreme brightness and rapid velocities produced images with a lower area boundary of ~5 μm^2. The brightest objects were identified from intensity histograms of all objects in the region of interest over the 2 min time course; threshold intensities were adjusted slightly from file to file to yield the greatest number of tracks with the lowest frequency of inappropriate joining of objects, but always excluded at least 90% of objects. Tracks containing fewer than 6 time points with trajectory velocities of less than 50 µm/s or total displacements of less than 5 µm were excluded, and the maximum distance between successive objects in a track was selected automatically in Volocity. The upper limit of detection in our bead tracking protocol was 940 µm/s, and the median bead velocity in these experiments over-represented the lowest shear stress conditions, where tracks were more abundant.

Tracking protocol for intravital microscopy time courses

The centroid-based tracking protocol and parameters measured for tracking of *B. burgdorferi*-endothelial interactions in time courses obtained by intravital microscopy were similar to the conditions for bead tracking, except that objects with areas between 5-400 μm^2 were tracked and trajectories with velocities >400 µm/s were excluded. The brightest ~10% of objects acquired at maximum laser intensity were tracked, and the maximum distance between successive objects in a track was set manually to 40 µm, as this value was not reliably selected by Volocity for *in vivo* time courses. Semi-automated tracking was considerably more challenging for *in vivo* than *in vitro* data for several reasons. Object identification was less efficient *in vivo* due to reduced optical clarity and lower signal to noise ratio resulting from autofluorescence of surrounding tissues compared to flow chamber data. The longitudinal axis of vessels rarely lay perfectly parallel to the plane of view, and the position of vessels in the plane of view was often not perfectly stable, due to movement associated with breathing. The changing intensity of bacteria which moved slightly above or below the plane of view reduced the likelihood that objects corresponding to these bacteria identified over successive time points would be accurately assembled into the

same trajectory by automated tracking. Tracking could be accurately performed *in vivo* if tracks were assembled by manually identifying the objects to be joined in each successive time point, but this process was prohibitively time-consuming.

Tracking protocols for bacterial interactions in flow chambers

Due to the large numbers of free-flowing bacteria and interactions observed for some bacterial strains *in vitro*, two protocols were used to obtain the maximum number of tracks in each flow chamber time course. Protocol 1 was optimized for tracking faster interactions and was similar to the algorithm used for capturing trajectories in intravital microscopy data except that tracks with velocities <5 μm/s and greater than 400 μm/s or total displacements of <15 μm were excluded, and the maximum distance between successive objects in a track was calculated automatically in Volocity. Protocol 2 was optimized for slower interactions, and was similar to Protocol 1, except that tracks >150 μm/s were excluded, minimum object area was changed to 1 μm^2, and no minimum track displacements or velocities were defined. Both protocols were applied to each dataset, and duplicate trajectories were removed by identification of tracks obtained for the same videos timepoints which had similar average velocities, skeletal length, displacement: bacterial length ratios, bond forces and time elapsed/time point. This combination of parameters clearly distinguished unique trajectories. Duplicate identification was performed at least twice for each experimental replicate by two individuals (total of 4 rounds of identification and verification).

TRAJECTORY ANALYSIS METHODS AND FORMULAS

Multiple parameters of interaction trajectories were measured and calculated from tracking data in Excel, using macros and spreadsheet templates containing all calculation formulas. Numbers of tracks and interactions analyzed for the experiments reported in each figure are provided in **Table S2**. Since tracking yielded hundreds of thousands of lines of data, the accuracy of these data was verified in multiple ways, including error-checking formulas built into spreadsheets, and manual line-by-line verification of all data by at least two individuals, conducted at least three times by each individual. To limit user error by due to repetitive procedures, macros and Excel template files were developed so that data could be imported directly from Volocity output files and analyzed in batches by experiment.

Track numbers and velocity (Fig. 1C-D)

Whole track velocity (**Fig. 1C**): total track displacement/total time elapsed over track. *Number of tracks/min* (**Fig. 1D**): numbers of unique tracks/min per time course, averaged over multiple replicates. Velocity and track numbers were calculated for all tracks with velocities ≤400 μm/s obtained at 0.5-3 dyn/cm^2.

Interaction cycle frequency, velocity and acceleration magnitude (Fig. 2C-D, 5C, J, 6E, S2A, S3A, S5F, I)

Average velocity, acceleration and frequency of each interaction cycle and acceleration and deceleration phases of interaction cycles were calculated per trajectory (per bacterium), then averaged over all tracks with velocities ≤400 μm/s obtained at 0.5-3 dyn/cm^2. Each acceleration and deceleration phase of a cycle corresponded to a group of time points in which the instantaneous velocities at each time point were greater than (acceleration) or less than (deceleration) the velocity of the preceding time point, as determined using conditional formulas. Since the instantaneous velocity of the first time point measured in each trajectory was often 0, the parameters for the first two time points in each trajectory were not included in interaction cycle analysis calculations.

Frequency (Fig. S2A)

Interaction cycle average: (number of acceleration and deceleration phases in each trajectory)/2*(sum of time elapsed in all acceleration and deceleration phases in each trajectory). *Acceleration phase average*: (number of acceleration phases in each trajectory)/(sum of time elapsed in all acceleration phases in trajectory). *Deceleration phase average*: (number of deceleration phases in each trajectory)/(sum of time elapsed in all deceleration phases of each trajectory).

Velocity (Fig. 2C, 5C, J, 6E, S3A, S5F, I)

Interaction cycle average: mean of all acceleration and deceleration phase velocities in each track. *Acceleration phase average*: mean of all acceleration phase velocities in each track. *Deceleration phase average*: mean of all deceleration phase velocities in each track. Velocities shown in **Fig. 5C, J, 6E and S5F and I** are deceleration phase velocities. In **Fig. S3A**, average cycle velocities for each track were plotted against shear stress for all interactions with velocities < and > 300 μm/s. Linear regressions and calculations of Spearman correlation coefficients were performed in GraphPad Prism v.6.04 (GraphPad Software, Inc., La Jolla, CA).

Acceleration magnitude (Fig. 2D)

Net acceleration/interaction cycle: change in velocity/change in time measured for each deceleration and acceleration phase in every track, averaged over all interaction phases in each track. *Acceleration phase average*: mean change in velocity/change in time for all acceleration phases in each track. *Deceleration phase average*: mean change in velocity/change in time for all deceleration phases in each track.

Lifetime analysis and calculation of interaction dissociation rates (K_{off}) (Fig. 2E-F, 5D, I, 6A-B, S2B-C, S5G)

As described (Sarangapani et al., 2004), the frequency of individual deceleration phase lifetimes (time elapsed during each deceleration phase) with a lifetime ≥ t was calculated all interactions obtained from 0.5-3 dyn/cm^2. The ln of the number of events with lifetime ≥t was plotted against lifetime t (100% of values analyzed for each curve). To determine if frequency distributions were linear or non-linear, best-fit curves were obtained by nonlinear regression analysis (least squares method) in GraphPad Prism, by comparing the fit of linear, hyperbola and one-phase exponential decay curves using the extra sum-of-squares F-test. Runs tests were performed for the resulting best-fit curve for each dataset to determine if deviation from the best-fit model was significant (all p-values for all runs tests were >0.05, indicating that deviation from best-fit models was not significant). R^2 values for resulting linear curves were ≥0.9. Interaction dissociation rates (K_{off}) were obtained from the negative slopes of linear curves fit to lifetime analysis data. Interaction

subsets analyzed in different experiments: **Fig. 2E-F, S2B-C:** All interactions with velocities ≤400 μm/s obtained for all lengths of bacteria from 0.5-3 dyn/cm^2; **Fig. 5D, I, 6A-B, S5G:** Interactions with velocities ≤300 μm/s and bacterial lengths under flow less than mean length of each strain under static conditions, obtained from 0.5-3 dyn/cm^2. In **Fig. 5I and 6A-B**, off-rates were calculated for interactions binned by bacterial length under flow, as described below. **In Fig. 6**, the population of interactions corresponding to the 2.83 μm bacterial length bin was divided into 4 groups by F_b value with equal numbers of interactions/group, in order to determine the bond force range over which dissociation rates and velocities for untethered interactions continued to slow.

Bacterial conformation parameters (Fig. 3B-D, F-H, S3B-E, all data binned by bacterial length, shear stress & F_b: 3D-E, H, 4C, E, 5G-J, 6A-E, S4B-C, G, S5I)

Bacterial length and diameter (Fig. 3B-E, H, 4C, E, 5G-J, 6A-E, S3B, D, S4B-C, F-G, S5I)

Measurements under no-flow (static) conditions (**Fig. S3B**)
Bacterial length and diameter were measured in 1min time lapse videos of live bacteria on endothelia in flow chambers, captured under static (no-flow) conditions. After tracking, the average skeletal length and skeletal diameter of each bacterium were calculated from all of the instantaneous values obtained in each trajectory (900 frames). Average values for each bacterium were used to calculate average length and diameter of populations for each strain. Measurements were performed with 3 independent bacterial cultures/strain, typically after completion of experiments conducted under flow. The standard deviation in length across all timepoints for each bacterium, which corresponds to the measurement error due to bacterial movement (contraction and extension) and computational errors in accurately defining the centroid position of bacteria was 10.45% of bacterial length, on the order of 1-2 μm/bacterium.

Bacterial length binning procedures for analyzing interactions under flow (**Fig. 3D-E, H, 4C, E, 5G-J, 6A-E, S4B-C, F-G, S5I**)
Interactions were binned into groups by bacterial length, with bin centers of 2.83, 5.66, 8.49, 11.32 and 14.15 μm. Binning of interactions by bacterial length was also used to calculate mean shear stress and F_b of interactions for each bacteria length bin, which were used for analyses plotting various parameters against shear stress (**Fig. 4E, 6A, C, S5I**) or F_b (**Fig 4E, 5G-J, 6B, D-E**).

Bacterial projection above endothelial surfaces (r) (Fig. 3F-H, S3C, E)
As described in **Fig. S3C**, the radius of bacteria projecting above endothelial surfaces (*r*) was determined by first calculating the average cylindrical volume of each bacterial strain from measurements of bacterial length under static conditions (**Fig. S3B**), and known values for the amplitude (1.11 μm: edge-on height) and thickness (0.33 μm: flat-on height) of the *B. burgdorferi* sine wave and body previously measured by electron microscopy (Goldstein et al., 1996). Formula: V=πr^2h, where *r* values for volume calculations were 0.555 and 0.165 μm, and h was no-flow bacterial length. The radius of bacteria projecting above surfaces (r) was then calculated by r = V/πLR, where V was the strain-specific volume of bacteria measured under static conditions, L was the instantaneous skeletal length of bacteria measured at each time point during deceleration, and R was ½ the instantaneous skeletal diameter of bacteria measured at each time point during deceleration. Average *r* values for each deceleration phase calculated from all timepoints within each phase were used to calculate interaction population means (**Fig. 3F, H**). In **Fig. 3F**, means were calculated for all interactions obtained from 0.5- 3 dyn/cm^2 with velocities <300 μm/s and all bacterial lengths. In **Fig. 3H**, means were calculated for all interactions obtained from 0.5- 3 dyn/cm^2 with velocities <300 μm/s binned by bacterial length. In **Fig. 3G and S3E**, instantaneous *r* values for each time point in each deceleration phase were plotted against cumulative interaction displacement at the same time point, for interactions with velocities <300 μm/s, to a maximum displacement of 50 μm (all bacterial lengths). Best-fit curves were obtained by nonlinear regression analysis (least squares method) in GraphPad Prism, by comparing the fit of linear, hyperbola, one-phase exponential decay and 4-phase sigmoidal curves using extra sum-of-squares F-tests and runs tests, after removal of 0.1% of outliers. Curves were weighted by 1/x^2.

Lengthwise deformation (Fig. 3B-D, S3D)
Lengthwise deformation index was calculated from instantaneous skeletal length: diameter ratios measured at each time point during each deceleration phase, and expressed as a percentage of skeletal length: diameter ratios measured for the same strain under static conditions. Average lengthwise deformation indices for each deceleration phase calculated from all timepoints within each phase were used to calculate interaction population means (**Fig. 3B, D**). In **Fig. 3B**, means were calculated for all interactions obtained from 0.5-3 dyn/cm^2 with velocities <300 μm/s and all bacterial lengths. In **Fig. 3D**, means were calculated for all interactions obtained from 0.5- 3 dyn/cm^2 with velocities <300 μm/s binned by bacterial length. In **Fig. 3C and S3D**, instantaneous deformation index values for each time point in each deceleration phase were plotted against cumulative interaction displacement at the same time point, for interactions with velocities <300 μm/s, to a maximum displacement of 50 μm (all bacterial lengths). Best-fit curves were obtained by nonlinear regression analysis (least squares method) in GraphPad Prism, by comparing the fit of linear, hyperbola, one-phase exponential decay and 4-phase sigmoidal curves using extra sum-of-squares F-tests and runs tests, after removal of 0.1% of outliers.

Displacement, displacement:bacterial length ratios, tether length (Fig. 3E, I-J, 5A, H, S5A, C-F)

Displacement (Fig. 3H, K, 5B, S5A, S5D)
In **Fig. 3E**, means were calculated for all interactions obtained from 0.5-3 dyn/cm^2 with velocities <300 μm/s, binned by bacterial length. Net conformational change-independent displacement (**Fig. 3I-J**) was calculated be measuring net change in skeletal (bacterial) length over all of the timepoints of each interaction phase, then subtracting this value from total displacement for the same phase. Calculations were performed for interactions obtained from 0.5-3 dyn/cm^2 with velocities ≤300 μm/s and displacement: bacterial length values of ≤1. In **Fig. 5A, S5A**, population means for total displacement during each deceleration phase were calculated for interactions with velocities ≤300 μm/s (all bacterial lengths). Displacement beyond no-flow bacterial length for strains (**Fig. 5A**) was calculated by subtracting their average bacterial length under static conditions (**Fig. S3B**) from total displacement of each interaction (**Fig. S5A**). At

the imaging acquisition framerate used for all experiments (15 fps), standard deviation in the length of live bacteria measured in the absence of flow was 10.45% of total length (on the order of 1-2 µm). Thus, variations in displacement due to measurement variation (and bacterial motility) were likely no greater than 2 µm.

Displacement: bacterial length ratios (**Fig. S5C-F**)
Displacement: bacterial length ratio calculations were performed for deceleration phase interactions obtained from 0.5-3 dyn/cm² with velocities ≤300 µm/s, and bacterial lengths under flow ≤ strain-specific average bacterial lengths under static conditions (**Fig. S3B**). Average displacement: bacterial length ratios for each interaction were obtained by averaging ratios calculated at each time point in each interaction, and were used for subsequent analyses based on this ratio. The frequency distribution of ratios obtained by this method was calculated in GraphPad Prism with a bin size of 0.5 (**Fig. S5C**). G1-G4 subpopulations identified in this frequency distribution (ratios: G1: <1.0; G2: 2.541; G3: 2.541-4.5; G4: >2.541) were used for calculation of subpopulation-specific velocities (**Fig. S5F**), displacement (**Fig. S5D**) and time elapsed/interaction (**Fig. S5E**). Interactions in population G1 were untethered (-T). Interactions in populations G2-G4 were tethered (+T).

Tether length (**Fig. 5H**)
As described in Fig. S5, tether length for interactions from 0.5-3 dyn/cm² with velocities ≤300 µm/s, and bacterial lengths under flow ≤ strain-specific average bacterial lengths under static conditions were calculated by identifying time points in each interaction where bacterial displacement: ratios were >1.0, and adding the distance travelled in each of these time points to obtain total tethered displacement, or tether length. Displacement attributed to tether extension was likely not due to dissociation rates that were more rapid than image acquisition, as dissociation rates estimated from interaction lifetimes were similar to or slower than acquisition framerate (**Fig. 5I**). To ensure that tether length calculations took into account bond dissociation rates, we estimated tether length by dividing the velocity of each interaction by the dissociation rates of interaction groups binned by bacterial wavelength. This procedure yielded lower estimates of tether length, but these lengths were still greater than the length of bacteria.

Force calculations (**Fig. 4A-E, 5E-J, 6A-E, S4A-I, S5I**)
Please see **Fig. 4A, S4A** for schematic illustration of parameters and equations referred to in this section, which have previously been described in detail (Alon et al., 1995; Sundd et al., 2011).

Bond angle (**Fig. S4F-I**)
Bond angle (θ) was calculated from $\cos\theta = l/R$, where l = bacterial displacement during deceleration, $R = \sqrt{r^2 + l^2}$, and r = radius of bacterial projection above endothelial surfaces. In **Fig. S4F**, instantaneous r values for each time point in each deceleration phase were plotted against cumulative interaction displacement at the same time point, for interactions with velocities <300 µm/s, to a maximum displacement of 50 µm (all bacterial lengths). Best-fit curves were obtained by nonlinear regression analysis (least squares method) in GraphPad Prism, by comparing the fit of linear, hyperbola, one-phase exponential decay and 4-phase sigmoidal curves using extra sum-of-squares F-tests and runs tests, after removal of 0.1% of outliers. Average r values for each deceleration phase calculated from all timepoints within each phase were used to calculate interaction population means (**Fig. S4G-I**). In **Fig. S4G**, means were calculated for all interactions obtained from 0.5- 3 dyn/cm² with velocities <300 µm/s binned by bacterial length.

Force on the bond (F_b), torque (T_s) and force (F_s) due to flow, shear stress (**Fig. 4B-E, 5E-J, 6A-E, S4B-E, S5I**)
Force on the bond (F_b) was calculated from $F_b = F_s/\cos\theta$, where force due to flow (F_s) = 31.97 $\tau_w r^2$, and τ_w is wall shear stress. Torque (T_s) =11.87 $\tau_w r^3$. Average F_b, T_s and F_s values for each deceleration phase calculated from all timepoints within each phase were used to calculate interaction population means (**Fig. 4B, 5E, S4D-E**). Average shear stress values (**Fig. 4D, 5F**) were calculated for the same interaction populations. In **Fig. S4B-C**, means were calculated for all interactions obtained from 0.5- 3 dyn/cm² with velocities <300 µm/s binned by bacterial length. Mean F_b and shear stress values obtained for individual bacterial length bins were used to plot other parameters (e.g. % interactions, K_{off}) against F_b and shear stress in **Fig. 4C, E, 5G-J, 6A-E, S5I**. **In Fig. 6**, the population of interactions corresponding to the 2.83 µm bacterial length bin was divided into 4 groups by F_b value with equal numbers of interactions/group, in order to determine the bond force range over which dissociation rates and velocities for untethered interactions continued to slow.

Bacterial propulsive force estimates (**Fig. 4C**)
For GCB966 and GCB971, which are ~13.4 µm long under no-flow conditions (**Fig. S3B**), *B. burgdorferi* propulsive force due to bacterial motility (F_m) was estimated from: $F_m \approx 4\pi$(bacterial length: 13.4 µm) (bacterial swim speed in liquid media with the viscosity of saline: 4.25 µm/s), and was ≈ 0.72 pN (Goldstein et al., 1994; Wolgemuth, 2008).

SUPPLEMENTAL REFERENCES

Alon, R., Hammer, D.A., Springer, T.A., 1995. Lifetime of the P-selectin-carbohydrate bond and its response to tensile force in hydrodynamic flow. Nature 374, 539–542. doi:10.1038/374539a0

Barbour, A.G., 1984. Isolation and cultivation of Lyme disease spirochetes. Yale J Biol Med 57, 521–5.

Bergström, S., Zückert, W.R., 2010. Structure, function and biogenesis of the *Borrelia* cell envelope, in: Samuels, D.S., Radolf, J.D. (Eds.), *Borrelia*: Molecular Biology, Host Interaction, and Pathogenesis. Caister Academic Press, Norfolk, UK, pp. 139–166.

Goldstein, S.F., Buttle, K.F., Charon, N.W., 1996. Structural analysis of the *Leptospiraceae* and *Borrelia burgdorferi* by high-voltage electron microscopy. J Bacteriol 178, 6539–45.

Goldstein, S.F., Charon, N.W., Kreiling, J.A., 1994. *Borrelia burgdorferi* swims with a planar waveform similar to that of eukaryotic flagella. Proc Natl Acad Sci U S A 91, 3433–7.

Moriarty, T.J., Norman, M.U., Colarusso, P., Bankhead, T., Kubes, P., Chaconas, G., 2008. Real-time high resolution 3D imaging of the Lyme disease spirochete adhering to and escaping from the vasculature of a living host. PLoS Pathog. 4, e1000090. doi:10.1371/journal.ppat.1000090

Moriarty, T.J., Shi, M., Lin, Y.-P., Ebady, R., Zhou, H., Odisho, T., Hardy, P.-O., Salman-Dilgimen, A., Wu, J., Weening, E.H., Skare, J.T., Kubes, P., Leong, J., Chaconas, G., 2012. Vascular binding of a pathogen under shear force through mechanistically distinct sequential interactions with host macromolecules. Mol. Microbiol. 86, 1116–1131. doi:10.1111/mmi.12045

Norman, M.U., Moriarty, T.J., Dresser, A.R., Millen, B., Kubes, P., Chaconas, G., 2008. Molecular mechanisms involved in vascular interactions of the Lyme disease pathogen in a living host. PLoS Pathog. 4, e1000169. doi:10.1371/journal.ppat.1000169

Sarangapani, K.K., Yago, T., Klopocki, A.G., Lawrence, M.B., Fieger, C.B., Rosen, S.D., McEver, R.P., Zhu, C., 2004. Low force decelerates L-selectin dissociation from P-selectin glycoprotein ligand-1 and endoglycan. J. Biol. Chem. 279, 2291–2298. doi:10.1074/jbc.M310396200

Seshu, J., Esteve-Gassent, M.D., Labandeira-Rey, M., Kim, J.H., Trzeciakowski, J.P., Höök, M., Skare, J.T., 2006. Inactivation of the fibronectin-binding adhesin gene *bbk32* significantly attenuates the infectivity potential of *Borrelia burgdorferi*. Mol Microbiol 59, 1591–1601. doi:10.1111/j.1365-2958.2005.05042.x

Sundd, P., Pospieszalska, M.K., Cheung, L.S.-L., Konstantopoulos, K., Ley, K., 2011. Biomechanics of leukocyte rolling. Biorheology 48, 1–35. doi:10.3233/BIR-2011-0579

Wolgemuth, C.W., 2008. Collective swimming and the dynamics of bacterial turbulence. Biophys. J. 95, 1564–1574. doi:10.1529/biophysj.107.118257

Wu, J., Weening, E.H., Faske, J.B., Hook, M., Skare, J.T., 2011. Invasion of eukaryotic cells by *Borrelia burgdorferi* requires β_1 integrins and Src kinase activity. Infect Immun 79, 1338–1348. doi:10.1128/IAI.01188-10

Zhi, H., Weening, E.H., Barbu, E.M., Hyde, J.A., Höök, M., Skare, J.T., 2015. The BBA33 lipoprotein binds collagen and impacts *Borrelia burgdorferi* pathogenesis. Mol. Microbiol. 96, 68–83. doi:10.1111/mmi.12921